Bi/UiO-66-derived electrocatalysts for high CO_2-to-formate conversion rate

Yuta Takaoka [a], Jun Tae Song [a,b,*], Atsushi Takagaki [a,b], Motonori Watanabe [a,b], Tatsumi Ishihara [a,b,*]

[a] Department of Applied Chemistry, Faculty of Engineering, Kyushu University, Motooka 744, Nishi-ku, Fukuoka 819-0395, Japan
[b] International Institute for Carbon-Neutral Energy Research (WPI-I2CNER), Kyushu University, Motooka 744, Nishi-ku, Fukuoka 819-0395, Japan

ARTICLE INFO

ABSTRACT

In the CO_2 electrocatalytic reduction reaction (CO_2RR) technology, high CO_2 conversion rate is highly required for efficient CO_2 utilization from the CO_2 resource. In this study, we propose the strategy of combining UiO-66 metal organic framework (MOF) structure with Bi electrocatalyst for highly active CO_2RR with selective formic acid production. The synthesized Bi/UiO-66 catalyst shows superior CO_2 reduction property, 4.6 times higher current density at −0.7 V vs. reversible hydrogen electrode (RHE) than bare Bi without UiO-66 despite of low electrochemical surface area. Also, NH_2 functionalized UiO-66 shows almost no effect on CO_2RR as compared to without NH_2 probably due to disassembled linkers during CO_2RR. Various characterizations such as Fourier transform infrared (FTIR), Raman spectroscopy, X-ray photoelectron spectroscopy (XPS) indicate carbonate species captured form of CO_2 at Zr-MOF site should contribute the high CO_2 conversion rate. Our findings demonstrate the feasibility of Zr-MOF as a Supporting material to achieve efficient CO_2 reduction.

1. Introduction

The efforts such as CO_2 utilization toward carbon neutrality has been gaining attention to avoid climate change caused by global warming. In particular, CO_2 electrocatalytic reduction reaction (CO_2RR) to value-added products using renewable energy has attracted great attention to address both CO_2 emission and the intermittency issue of renewable energy sources. However, CO_2RR technology faces some challenges as follows: large overpotential [1,2], inevitable hydrogen (H_2) evolution reaction (HER) by water reduction [3], and low CO_2 conversion rate [4–6]. Although many previous research with Ag [7], Cu [8–10], Au [11, 12], Pd [13,14], Bi [15,16], etc. could not achieve satisfactory performance in terms of current density, selectivity and durability, recent works for the production of formic acid (HCOOH) which can serve as a H_2 carrier are receiving great attention with its advanced catalytic activity [17–21]. Among CO_2RR catalysts for HCOOH production such as In [22–25], Pb [26,27], Sn [28–30], Pd [31,32] and Bi [15,16,33–44], Bi has attracted much attention because of its high selectivity for HCOOH, low cost, and low toxicity [37]. Despite of the improved catalytic activity, it is urgent to develop for achieving economically viable level.

Recently, metal-organic framework (MOF) has attracted attention as platforms due to its special features of photo-responsivity, high surface area and versatile porosities which are advantageous for various applications such as photocatalysts [45–51], gas storage materials [52], and separation membranes [53,54]. Despite of electrically insulating property, MOF materials have been successfully utilized for electrocatalysts [55]. Nam et al. established Ag-decorated Zr-MOF (UiO-66) for enhanced CO_2 reduction to CO. It was found that binding energy of intermediate species of CO_2 reduction reaction process could be controlled by the linker or metal node [47]. However, the achieved current density is not satisfactory level despite of operating with flow-cell environment. On the other hand, some efforts have been focused on the use of 2D conjugated MOFs or structural transformation of MOFs for higher electrical conductivity. For example, phthalocyanine-based bimetallic 2D conjugated MOF (PcCu-O8-Zn) synthesized with copper-phthalocyanine as ligand (CuN_4) and zinc-bis (dihydroxy) complex (ZnO_4) as linkage was reported to show successful electrocatalytic property with high CO selectivity of 88 % by CO_2 electrolysis [56]. In addition, Li et al. developed ligand-stabilized Bi nanosheets by electrochemically reducing MOF structure for CO_2 reduction to formic acid [37]. Meanwhile, ZrO_2 has been widely used for CO_2 reduction because it has plenty of CO_2 adsorption sites such as Bronsted acidic and basic hydroxyl groups and unsaturated Lewis acidic Zr^{4+} cations [9,57]. Inspired by these works, we anticipated that transformation of zirconium-based benzenedicarboylate MOF (UiO-66) structure should be a strategy to not only increase electroconductivity but also efficiently utilize Zr

functional sites for CO_2 activation.

Herein, we rationally developed Bi/UiO-66-derived electrocatalysts for enhancing electrochemical CO_2 reduction to HCOOH. In fact, it was reported that UiO-66 shows structural breakdown into $Zr_6O_4(OH)$ under basic condition [58]. Taking this property of UiO-66, we synthesized the electrocatalysts by KOH treatment for 5 min on Bi deposited UiO-66 samples to achieve high conductivity. The crystallinity of UiO-66 is lost after KOH treatment indicating structural evolution of UiO-66. However, Bi nanoparticles are still attached exterior to the cubic-shaped UiO-66 site. As the results, the prepared Bi/UiO-66 samples exhibit high CO_2RR activity for formic acid production with about 80 % Faraday efficiency for formic acid in the potential range from -0.4 V to -0.7 V (vs. reversible hydrogen electrode (RHE)). In particular, the current density for Bi/UiO-66-derived sample is $\sim 4 \sim 5$ times improved as compared to synthesized Bi sample by same method of Bi/UiO-66 despite of identical electrochemical active surface area (ECSA). Also, amine (NH_2) functionalized UiO-66 (UiO-66-NH_2) shows slightly higher activity than UiO-66 sample. Various characterizations such as Fourier transform infrared (FTIR), Raman spectroscopy and X-ray photoelectron spectroscopy (XPS) suggest the interaction between Zr-MOF and carbonate should be key factor to increase CO_2 conversion rate.

2. Experimental method

2.1. Preparation of UiO-66

UiO-66 was synthesized by following a method reported on previous literature [59]. After dissolving 200 mg of 1,4 benzenedicarboxylic acid (BDC) (Tokyo Chemical Industry, Japan, $>$ 99.0 %) in 140 mL of *N,N*-dimethylformamide (DMF) (FUJIFILM Wako Pure Chemical Corporation, Japan, $>$ 99.5 %), 14 mg of triethylamine (TEA) (Kishida Chemical, Japan, $<$99.0 %) was added. After stirring it, acetic acid (CH_3COOH) (FUJIFILM Wako Pure Chemical Corporation, Japan, $>$ 99.7 %) of 20 mL was added. The mixture was then moved to the flask and heated up to 120 ℃. Then, to this preheated mixture, 280 mg of zirconium chloride ($ZrCl_4$) (Nacalai tesque, Japan, $>$ 97.0 %) dissolved in 140 mL of DMF was added. The mixture was kept at 120 ℃ for 6 h in oil both. After 6 h, the solution was centrifuged to collect UiO-66 and it was washed several times (more than 3 times) with DMF and EtOH (Kishida Chemical, Japan, $>$ 99.5 %). Finally, UiO-66 powder of about 300 mg was collected after vacuum drying at 80 ℃ overnight.

2.2. Preparation of UiO-66-NH_2

UiO-66-NH_2 was synthesized by following a reported method with a slight modification.[53] After dissolving 216 mg of 2-aminoterephthalic acid (Tokyo Chemical Industry, Japan, $>$ 98.0 %) in 140 mL of DMF, 28 mg of TEA was added. These were added with CH_3COOH of 20 mL during stirring. The mixture was transferred to a flask and heated up to 120 ℃. 280 mg of $ZrCl_4$ dissolved in 140 mL of DMF was added to the preheated mixture. Then, the mixture was heated at 120 ℃ for 6 h in oil bath. After heating at 120 ℃, the reaction solution was centrifuged to collect UiO-66-NH_2, then washed several times (more than 3 times) with DMF and EtOH. UiO-66-NH_2 collected was vacuum-dried at 80 ℃ for overnight. The yield of UiO-66-NH_2 was about 350 mg.

2.3. Bi deposition on UiO-66 MOFs

Bi was deposited on MOF structure by chemical reduction method of bismuth nitrate pentahydrate ($Bi(NO_3)_3 \cdot 5H_2O$) (FUJIFILM Wako Pure Chemical Corporation, Japan, $>$ 99.9 % and Kishida Chemical, Japan, $>$ 99.5 %). First, 0.10 mmol of $Bi(NO_3)_3 \cdot 5H_2O$ was dissolved in 10 mL of acetone with sonication. 100 mg of MOFs (UiO-66 and UiO-66-NH_2) were added into $Bi(NO_3)_3 \cdot 5H_2O$ dissolved acetone with stirring for 6 h at room temperature. The mixture of UiO-66 and $Bi(NO_3)_3 \cdot 5H_2O$ was centrifuged and vacuum-dried at 80 ℃ overnight. Collected mixture powder was crushed and added to 6 mmol sodium borohydride ($NaBH_4$) (Tokyo Chemical Industry, Japan, $>$ 95.0 %) dissolved 10 mL EtOH solution. Then, it was kept for reduction reaction for 5 min with stirring. The composite materials were centrifuged to collect, then washed several times (more than 3 times) with dehydrated EtOH. Finally, it was vacuum-dried at 80 ℃ overnight and crushed.

2.4. Preparation of Bi powder

Bi particle sample for comparison was synthesized without MOF samples by $NaBH_4$ reduction without MOF powders. We carried out same procedure to obtain Bi particle samples for Bi deposition on MOF by preparing 3.0 mmol of $Bi(NO_3)_3 \cdot 5H_2O$ dispersed in 10 mL acetone. Then, collected mixture powder was crushed and added into 6 mmol $NaBH_4$ dissolved 10 mL EtOH solution. Then, it was kept for reduction reaction for 5 min with stirring. The composite materials were centrifuged to collect and washed several times (more than 3 times) with dehydrated EtOH. Finally, it was vacuum-dried at 80 ℃ overnight.

2.5. Preparation of electrodes with catalysts

Gas diffusion electrodes (GDE) with catalytic materials were fabricated by drop-casting method. First, catalysts ink was prepared by dispersing 40 mg of synthesized catalysts (15 mg in case of Bi powder sample) and 200 μL of 5 % Nafion dispersion solution (Alfa Aesor) in 2 mL of isopropyl alcohol (IPA) with 30 min sonication. The prepared catalyst ink was dropped on carbon paper (MGL280, AvCarb) which is gas diffusion layer (GDL) and dried for 10 min on the hot plate at 100–120 ℃. Before electrolysis test, all prepared electrodes (Bi/UiO-66, Bi/UiO-66-NH_2 and Bi) were treated by flowing 1.0 M KOH aqueous solution to the surface for 5 min in the flow-cell reactor which is for CO_2 electrolysis test. After this treatment, flow-cell reactor was washed to clean inside before CO_2 electrolysis test.

2.6. CO_2 electrolysis test

CO_2RR test was performed with gas flow type flow-cell [60]. The structure of flow-cell was constructed with anion exchange membrane (Selemion, AGC) sandwiched between cathode and anode chambers. The cathode side was set with the prepared GDE sample and a NiFeMo foil was utilized for anode. Ag/AgCl in saturated KCl aqueous solution was used for reference electrode. After assembling all parts of flow-cell, 1.0 M KOH aqueous solution was circulated to both cathode and anode chambers with a flow rate of 15 cc/min by peristaltic pump (Masterflex L/S). Then, CO_2 gas was flowed to GDL side via gas flow chamber located behind cathode chamber with flow rate of 20 cc/min. For electrochemical measurements such as cyclic voltammetry (CV), chronoamperometry and etc., we employed potentiostat instrument (SP-150, Bio-Logic Science Instruments Ltd). We note that CO_2RR tests were performed with 85 % IR-correction for various potential ranges. As the products analysis, gas products (H_2 and CO) were detected by micro gas chromatography (GC) equipped with molecular sieve column and thermal conductivity detector (TCD) (Micro GC 3000, Inficon) and HCOOH amount was quantified by high-performance liquid chromatography (HPLC) (LC02000 plus, JASCO) equipped with a differential refractive index detector (RI-2031 plus, JASCO) with an Aminex HPX-87 H column (flow rate: 0.5 cc/min, eluent: 10 mM H_2SO_4). Prior to liquid sample injection to HPLC, we diluted the electrolytes after CO_2 reduction test depending on the passed amount of charge for obtaining proper concentration. In addition, we repeated CO_2 electrolysis test at specific potentials with fresh samples for 3 times to verify the experimental results.

2.7. Electrochemical active surface area (ECSA)

CV tests were conducted in the potential range from 0.2 to 0.3 V (vs.

RHE) at various sweep rates of 20, 40, 60 and 80 mV/s with 20 times repetitions in 1.0 M KCl aqueous solutions to prevent structural change of Zr-MOF samples. Then, the capacitive current difference of $\Delta J(J_a - J_b)$ at a potential of 0.25 V (vs. RHE) was obtained [37,61]. The ΔJ vs sweep rates graph was plotted for double-layer capacitance (C_{dl}) was calculated from the slope obtained from the plot. Then, ECSA values were estimated for the reaction surface area on electrocatalysts [37,61].

2.8. Material characterizations

Powder X-ray diffraction (XRD) (RINT-2500HLR, Rigaku) with Cu Kα radiation at 40 kV and 80 mA and thin film XRD (SmartLab 9 kW AMK, Rigaku) with Cu Kα radiation at 45 kV and 200 mA were recorded to characterize the crystallinity of synthesized samples. Scanning electron microscopy (SEM) (JSM-7900F, JEOL) and transmission electron microscopy (TEM) or scanning transmission electron microscopy (STEM) (JEM-ARM200F, JEOL) at an acceleration voltage of 200 kV were carried out for the structural analysis. Energy dispersive X-ray (EDX) analysis was also accompanied with SEM and STEM. In detail, to obtain Bi/Zr contents ratio, we calculated the average ratio by measuring at least 3 spots by SEM-EDX. Fourier transform Infrared spectroscopy (FTIR) (FT/IR-610, JASCO) was conducted with attenuated total reflection (ATR) methods. Raman spectroscopy was carried out by inVia Raman microscope (Renishaw). The X-ray photoelectron spectroscopy (XPS) measurement was performed with Kratos Ultra2 (KRATOS) using Al-Kα radiation as the X-ray source. To correct the binding energy, Au 4f (84.0 eV) was utilized by slightly coated Au particles on the catalyst. For the detection of electrolyte contents, inductively coupled plasma (ICP) (Optima 5300 DV, PerkinElmer) analysis was utilized after CO_2 reduction reaction.

3. Results and discussion

3.1. As-synthesized electrocatalysts characterization

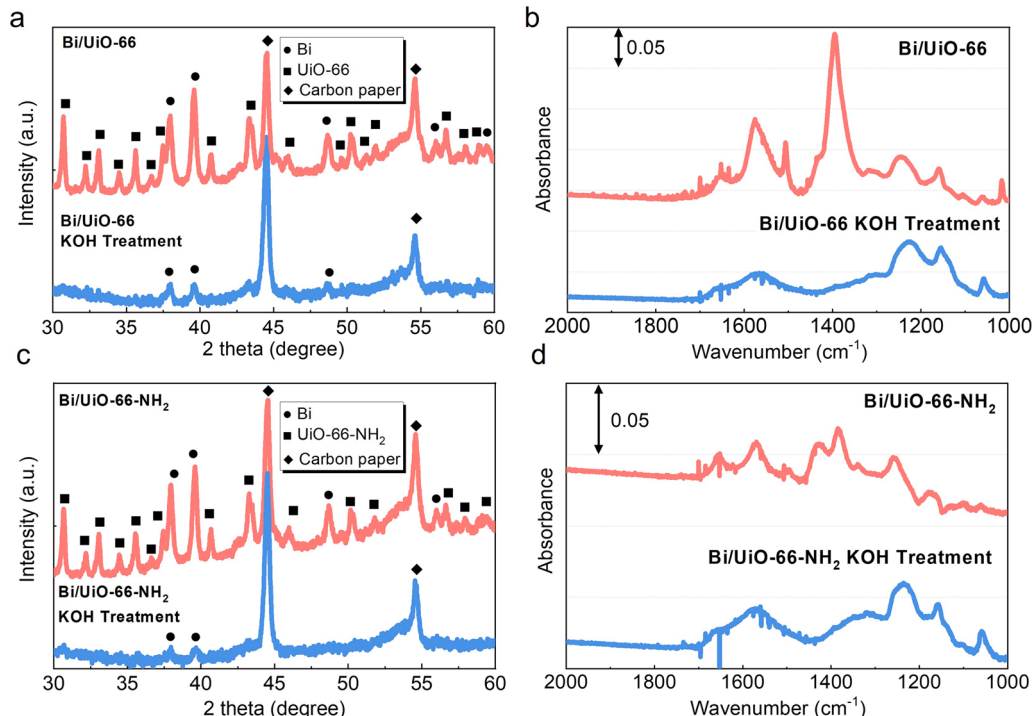The UiO-66 MOF was basically synthesized by following the method

of Zhao et al. with a slight modification [59]. Then, Bi was deposited on MOF samples by $NaBH_4$ reduction method. Fig. 1a shows the XRD patterns of the GDE samples coated with Bi/UiO-66 powders before and after KOH treatment. As-prepared Bi/UiO-66 shows XRD patterns for the combination of UiO-66 (CCDC number: 1018045) and metallic Bi (See Fig. S1 for XRD pattern of pristine UiO-66). FTIR spectra in Fig. 1b confirms major peaks from organic linker (BDC) for UiO-66. For example, the bands centered at 1015, 1395, 1504, 1576 and 1652 cm^{-1} reflect benzene ring deformation, C-O stretching, aromatic C-C ring stretching, O-C=O symmetric stretching and C=O stretching of the carbonyl group, respectively [62–65]. Also, in FTIR result, there have been several satellite peaks such as Nafion peaks at 1062 cm^{-1} (S-O stretching), 1159 cm^{-1} (C-F stretching) and 1243 cm^{-1} (C-F stretching) [66–68]. These observations indicate UiO-66 is well synthesized [63]. We also prepared functionalized UiO-66 with NH_2 (UiO-66-NH_2) by following the method of Sun et al. [53]. XRD and FTIR verify the successful synthesis of UiO-66-NH_2 (CCDC number for XRD: 1405751) (Fig. 1c and d). In comparison to UiO-66, UiO-66-NH_2 sample shows the characteristic peaks at 1259 cm^{-1} and 1341 cm^{-1} from C-N stretching of the aromatic ring and the peak at 3350 and 3592 cm^{-1} from stretching of the amino group (See Fig. S1 for higher wavenumber range of FTIR results) [65,69–71]. Then, we performed KOH treatment for Bi/UiO-66 and Bi/UiO-66-NH_2 samples by immersing in 1.0 M KOH solution for 5 min. Both UiO-66 samples were confirmed to undergo structural evolution during KOH treatment process. First of all, no XRD patterns for UiO-66 and UiO-66-NH_2 are shown while the peaks for metallic Bi and carbon paper are remained suggesting the crystallinity of UiO-66 and UiO-66-NH_2 was lost after KOH (Fig. 1a and c). Also, FTIR results show the major peaks originated from organic linkers are disappeared or significantly reduced for both Bi/UiO-66 and Bi/UiO-66-NH_2 indicating disassembly of Zr-MOF structures occurs with KOH treatment (Fig. 1b and d). It was also confirmed that UiO-66 structure is evidently changed to amorphous by directly dipping the prepared UiO-66 powder samples in KOH for 60 min (Fig. S2).

Then, we investigated the morphological characterization by SEM observation as shown in Fig. 2. Both pristine Bi/UiO-66 and Bi/UiO-66-
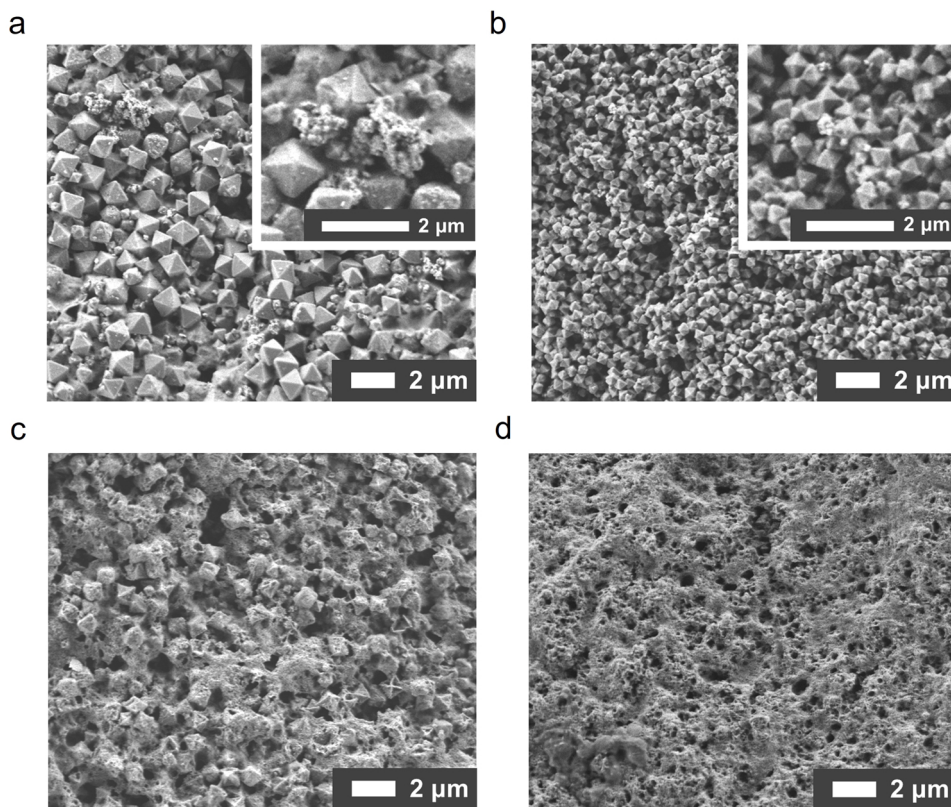

Fig. 1. Characterization results of synthesized Bi/UiO-66 and Bi/UiO-66-NH_2 materials before and after KOH treatment. (a) XRD diffraction patterns and (b) FTIR spectra of Bi/UiO-66 samples. (c) XRD diffraction patterns and (d) FTIR spectra of Bi/UiO-66-NH_2 samples.

Fig. 2. SEM images for (a) pristine Bi/UiO-66 with magnified view for Bi particles, (b) pristine Bi/UiO-66-NH$_2$ with magnified view for Bi particles, (c) KOH-treated Bi/UiO-66 and (d) KOH-treated Bi/UiO-66-NH$_2$.

NH$_2$ (before KOH treatment) with octahedral structures are coated on carbon cloth. For both pristine samples (Fig. 2a and b), clustered Bi particles are shown on Zr-MOF particles which is also confirmed with EDX analysis (Fig. S3). The Bi/Zr-MOF structure is also clearly observed by TEM (Fig. S4 and S5). After KOH treatment (Fig. 2c, d and Fig. S4b), it is obviously shown that both UiO-66 and UiO-66-NH$_2$ undergo structural evolution. Despite Bi particle is not clearly visible in SEM image because Bi particles are surrounded by Zr-MOF structures, EDX mapping results (See Fig. S3b and d for EDX mapping of KOH-treated samples) show Bi particles are more uniformly distributed on the surface than pristine samples. It indicates that Bi particles are physically moved for uniform distribution during KOH treatment. However, Bi/Zr atomic ratio measured by EDX measurement is not significantly changed for KOH-treated samples (21 % for Bi/UiO-66, 20 % for Bi/UiO-66-NH$_2$) as compared to pristine samples (19 % for Bi/UiO-66, 14 % for Bi/UiO-66-NH$_2$).

3.2. Electrocatalytic CO$_2$ reduction performance

Then, we performed CO$_2$ electrolysis experiments with flow-cell configuration to investigate the electrochemical CO$_2$ reduction activity of the synthesized samples (See Fig. S6 for the schematic of flow-cell configuration). Fig. 3a shows LSV results in comparison with under Ar or CO$_2$ gas flow. It is obvious that CO$_2$ gas flow allows largely increased current densities for both Bi/UiO-66 and Bi/UiO-66-NH$_2$ samples whereas almost negligible current density is obtained under Ar flow. This result suggests that Bi/UiO-66 and Bi/UiO-66-NH$_2$ exhibit high CO$_2$ reduction reactivity. When it compares between Bi/UiO-66 and Bi/UiO-66-NH$_2$, Bi/UiO-66-NH$_2$ shows slightly higher current density than sample without NH$_2$ group. For example, NH$_2$ functionalized one has −79 mA cm^{-2} at −0.5 V vs. RHE which is larger than −55 mA cm^{-2} for Bi/UiO-66. Then, I-V curves for each potential were obtained via chronoamperometry method as shown in Fig. 3b (See Fig. S8 for

chronoamperometry results at each potential). Note that average current density values are plotted at each potential. During electrolysis test, current density levels are mostly stable despite current density for Bi/UiO-66-NH$_2$ and Bi at −0.7 V vs. RHE is slightly decreased. Here, for the comparison, we also prepared Bi particle samples without MOF support via same NaBH$_4$ reduction method with Bi deposition on MOFs. As the results, Bi with UiO-66 and UiO-66-NH$_2$ samples exhibit much higher current density than Bi samples all over the potentials range. Particularly, the current density of Bi/UiO-66 is recorded to about −265 mA cm^{-2} at −0.7 V vs. RHE which is ~4.6 times improved as compared to Bi. Moreover, Bi/UiO-66-NH$_2$ exhibits slightly improved current density (−265 mA cm^{-2} at −0.7 V vs. RHE) than without NH$_2$ functional group. However, onset potentials of only Bi, Bi/UiO-66 and Bi/UiO-66-NH$_2$ for CO$_2$RR are similar, about −0.4 V vs. RHE indicating overpotential is not changed with Zr-MOF structures. Also, Faraday efficiency (FE) of formic acid for all samples are recorded to around 65 – 85 % in the potential range from −0.4 V to −0.7 V vs. RHE (Fig. 3c). FE values for other products such as H$_2$ and CO are consistently below ~10 % in total regardless of applied potentials (Fig. S8). Also, pristine UiO-66 after KOH treatment was tested to clarify whether it shows CO$_2$RR activity or not (Fig. S9). Although it exhibits about small amount of HCOOH with FE of 22 % at −0.7 V vs. RHE, only H$_2$ was found as a product −0.5 V vs. RHE. total FE below 20 % at −0.5 V vs. RHE indicates the reduction of Zr hydroxide from transformed Zr-MOF can occur in this potential region [72] It might be attributed to large error range in ± 20 % for FE for formic acid. Then, Tafel analysis of Fig. 3d shows Tafel slopes of all samples are 149 ~ 166 mV dec^{-1} indicating the rate-determining step of CO$_2$RR is initial step of first electron transfer forming CO$_2$ radical [73]. These results indicate that the utilization of UiO-66 as supporting materials for Bi catalysts particularly contributes to improve CO$_2$RR current density which is related to productivity. It is impressive that our achieved current density > 200 mA cm^{-2} at −0.7 V vs. RHE) is comparable to recent state-of-art results for Bi catalysts)

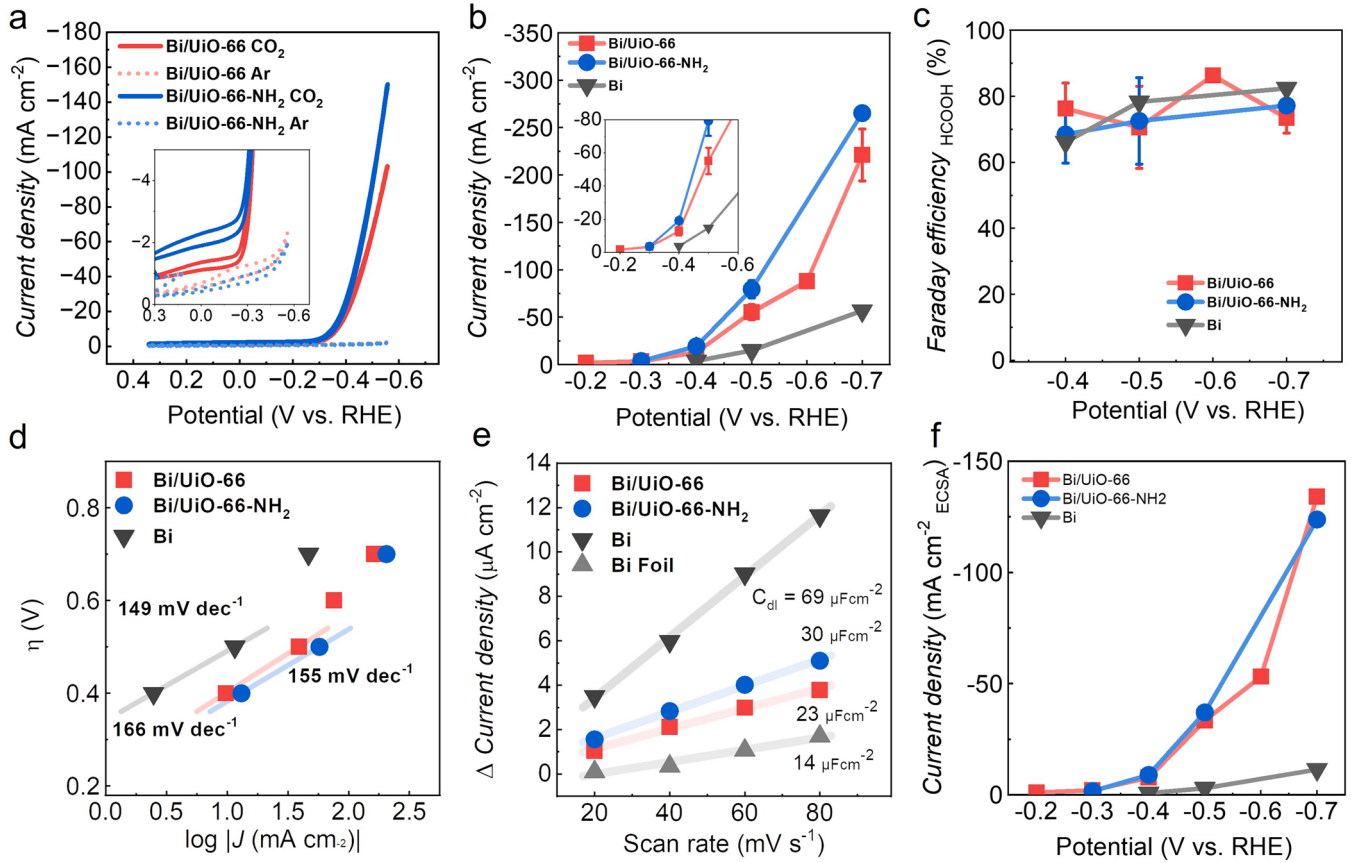**Fig. 3.** Electrochemical CO_2 reduction activity evaluation. (a) Linear sweep voltammetry (LSV) curves for Bi/UiO-66 and Bi/UiO-66-NH_2 in comparison of CO_2 or Ar gas flow. I-V graph under Ar flow is magnified as shown in inset graph. (b) Potential-dependent current density property of Bi/UiO-66, Bi/UiO-66-NH_2 and only Bi catalyst. Inset is magnified graph for low potential region. (c) Faraday efficiency plot of formic acid formation on Bi/UiO-66, Bi/UiO-66-NH_2 and only Bi catalyst. (d) Tafel plot at different overpotentials (η) as a function of partial current density for formic acid on Bi/UiO-66, Bi/UiO-66-NH_2 and Bi. Tafel slope is indicator for the rate determining reaction step. (e) Double-layer capacitive current density difference at 0.25 V vs. RHE versus scan rates of cyclic voltammetry (CV) measurement to estimate electrochemical surface area (ECSA). The slope indicates electric double layer capacitance (C_{dl}) which is related to ECSA. (f) The comparison of ECSA-normalized current density versus applied potentials.

because we synthesized Bi by simple $NaBH_4$ reduction method. (See Table S1 for benchmark of CO_2 reduction activity for Bi).

As an attempt to confirm the surface area effect for increased current density, we evaluated ECSA for all synthesized electrodes after KOH treatment by CV measurement (Fig. 3e and Fig. S10). As compared to Bi foil which has flat surface, all our synthesized samples of Bi, Bi/UiO-66 and Bi/UiO-66-NH_2 are revealed to have 4.9, 1.6 and 2.1 times larger ECSA values, respectively. Note that pristine UiO-66 has similar ECSA value with flat Bi foil indicating no significant effect ECSA measurement (Fig. S11). In particular, even though the particle size of Bi sample (Fig. S12) seems to be much larger than Bi/UiO-66 and Bi/UiO-66-NH_2, it has larger ECSA which is more advantageous for providing catalyst surface sites. Low ECSA for Zr-MOF samples should be attributed to surrounded Bi particles by structurally evolved Zr-MOF which is not highly electrically conductive. As the results, Bi with Zr-MOF samples exhibit much higher ECSA-normalized current densities than only Bi as displayed in Fig. 3f. Thus, the increased current density with UiO-66 and UiO-66-NH_2 should not be attributed to surface area effect implying that UiO-66 materials has critical role for higher CO_2 reduction current density. Meanwhile, in comparison between UiO-66 and UiO-66-NH_2, there is no noticeable difference in ECSA-normalized current density. As confirmed in FTIR (Fig. 1b and d), disassembled linkers from the Zr-MOF after KOH treatment might rarely affect CO_2 reduction activity. That is, the enhanced CO_2RR current density should be affected by the existence of Zr site of both UiO-66 and UiO-66-NH_2 rather than functional group type of organic linkers.

3.3. Electrocatalysts characterization after CO_2 electrolysis

In order to further understand the origin of improved CO_2 reduction activity with UiO-66, SEM, Raman and FTIR spectroscopy were carried out to characterize the Bi/UiO-66 sample after CO_2 electrolysis. Note that we focused only Bi/UiO-66 sample for characterization after CO_2RR due to negligible effect of NH_2-functionalized sample. Fig. 4a and b show the SEM plan-view for Bi/UiO-66 samples after CO_2RR for 960 s under the applied potentials of −0.5 V and −0.7 V vs. RHE, respectively (See Fig. S8 for electrolysis reaction test). At −0.7 V vs. RHE, surface condition is much severely changed than −0.5 V vs. RHE, implying CO_2RR promotes the structural evolution of Zr-MOF. After reaction for both −0.5 V and −0.7 V vs. RHE, Bi ratio compared with Zr is 23 % and 30 %, respectively. Only −0.7 V CO_2RR increases Bi contents as compared KOH treated Bi/UiO-66 of 22 % (See Fig. S13 for EDX analysis results before and after CO_2RR). Fig. 4c shows FTIR spectra for spent Bi/UiO-66 samples at −0.7 V vs. RHE. Although KOH-treated Bi/UiO-66 samples do not exhibit major peak at 1394 and 1588 cm^{-1} coming from organic linker, major peaks at 1321 cm^{-1} are clearly observable on Bi/UiO-66 sample after reaction. It implies Bi/UiO-66 compound structure is transformed to different form during CO_2RR. Chu et al. recently reported that UiO-66 can be digested into the form of $[Zr_2(OH)_2(CO_3)_4]^{2-}$ by bicarbonate as following chemical reaction [74].

$$Zr_6O_4(OH)_4(BDC)_6 + 18HCO_3^- \rightarrow 3[Zr_2(OH)_2(CO_3)_4]^{2-} + 8H_2O + 6CO_2 + 6BDC^{2-} \tag{1}$$
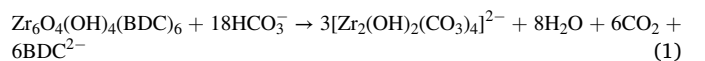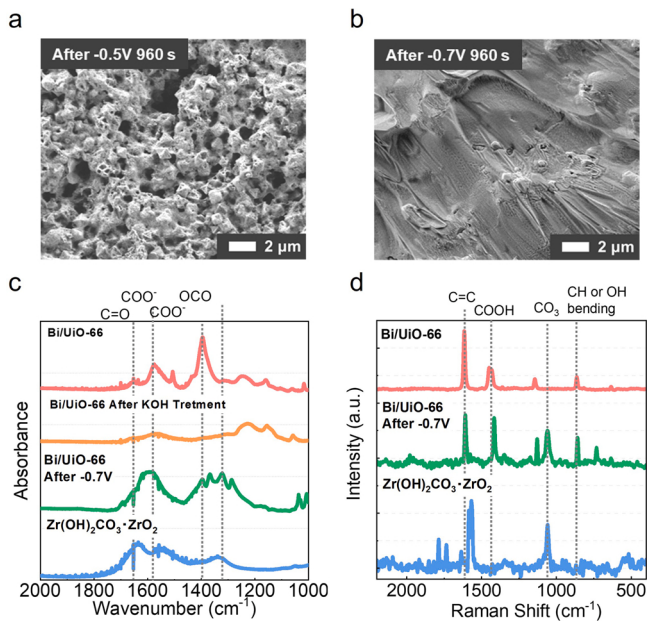
Fig. 4. SEM plan-view of Bi/UiO-66 samples surface after CO$_2$ electrolysis for 960 s at (a) −0.5 V and (b) −0.7 V vs. RHE. (c) FTIR analysis spectra of Bi/UiO-66 samples (pristine, KOH-treated and after CO$_2$RR for 960 s at −0.7 V vs. RHE) and Zr(OH)$_2$CO$_3$ · ZrO$_2$ sample for comparison. (d) Raman spectra of Bi/UiO-66 samples before and after CO$_2$RR for 960 s at −0.7 V vs. RHE and Zr(OH)$_2$CO$_3$ · ZrO$_2$ sample.

Thus, commercially available Zr(OH)$_2$CO$_3$ · ZrO$_2$ was also measured for the comparison. In FTIR spectrum of Zr(OH)$_2$CO$_3$ · ZrO$_2$ sample, the peak for O-C-O stretching in carbonate species is clearly shown at 1340 cm^{-1} [75,76]. This peak is also confirmed on the spent Bi/UiO-66 sample at −0.7 V vs. RHE. Raman spectroscopy provides obvious proof for the existence of carbonate species on sample after CO$_2$RR. After electrolysis for 960 s, Bi/UiO-66 sample's Raman spectrum is still mostly similar to pristine sample. However, the peak relevant to carbonate species which is also observable on Zr(OH)$_2$CO$_3$ · ZrO$_2$ at Raman shift of 1058 cm^{-1} is noticeably evolved [75]. According to these results, it is interpreted that carbonate species should be formed with transformed UiO-66 structures during CO$_2$ electrolysis in KOH solution.

Long-term CO$_2$RR operation test at an applied potential of −0.5 V vs. RHE for 4100 s with Bi/UiO-66 was conducted to investigate the difference on degraded samples with active state as shown in Fig. 5a (See Fig. S14a for the total current density behavior). During this long-term test, we monitored the linear increase of HCOOH production with reaction time (See Fig. S14b for time course of HCOOH production and S15 for HPLC chromatograms). Partial current density for HCOOH (j_{HCOOH}) reaches peak value (−59 mA cm^{-2}) at about 600 s, and then it gradually decreases to 68 % (−40 mA cm^{-2}) at 4100 s. Here, we first analyzed the samples at initial, 960 s and 4100 s with ex-situ XPS measurement to trace the surface chemical states. It is confirmed that Bi elements for all samples studied herein have identical oxidation states (Fig. 5b). However, Zr 3d spectra show the difference by samples condition as shown in Fig. 5c. The binding energy of peak center is shifted to lower energy (182.7 eV → 182.2 eV) for KOH-treated one and the sample after CO$_2$RR for 960 s. In fact, the peak position is close to the Zr(OH)$_4$ and Zr(OH)$_2$CO$_3$ · ZrO$_2$ (See Fig. S16 for Zr 3d peaks of Zr(OH)$_4$
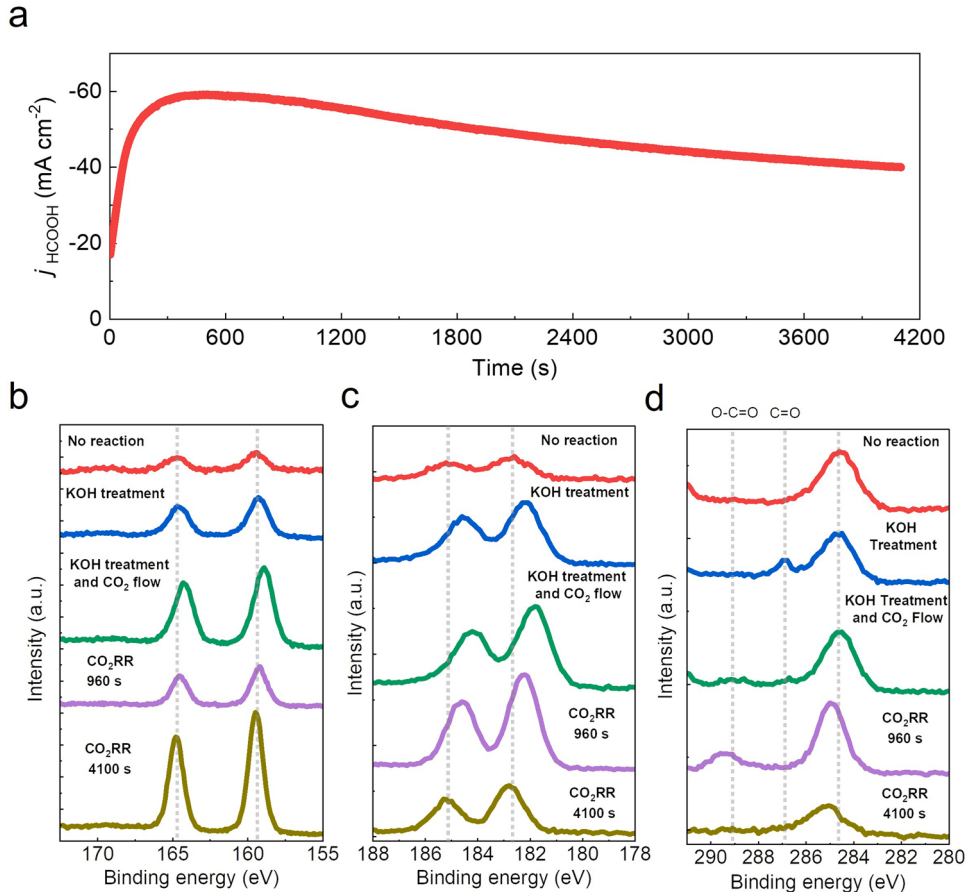

Fig. 5. (a) time course of partial current density for HCOOH (j_{HCOOH}) for Bi/UiO-66 during long-term CO$_2$ reduction operation at −0.5 V vs. RHE for 4100 s. Ex-situ XPS spectra of (b) Bi 4 f, (c) Zr 3d and (d) C 1 s for the Bi/UiO-66 samples of pristine state, KOH-treated before and after CO$_2$ flow, after reaction at −0.5 V vs. RHE for 960 s and 4100 s.

and $Zr(OH)_2CO_3 \cdot ZrO_2$) implying disassembled UiO-66 transformed in the form of zirconium hydroxide-related material as described in reaction Eq. (1) [74]. Interestingly, the peak position returns to 182.8 eV after CO_2RR for 4100 s. This phenomenon gives a hint regarding the activity improvement that transformed UiO-66 into Zr hydroxide compound should contribute the catalytic performance. Moreover, the role of carbonate species is revealed to be significant for CO_2RR activity via the comparison of C 1 s peaks. Even though carbonate relevant peak (O-C=O) at 289.2 eV is not observable before flowing CO_2 gas [77], initial state (after flowing CO_2 gas before starting electrolysis) and the state after 960 s CO_2RR show prominently evolved carbonate peak. Importantly, when the CO_2RR activity of electrocatalyst is degraded to $\sim$68 % after 4100 s CO_2RR, carbonate peak almost disappears suggesting carbonate has critical role for enhanced CO_2 reduction current density.

On the other hand, we also investigated the electrolyte contents and morphological change after CO_2RR to clarify other possible reasons for the degradation of j_{HCOOH}. ICP analysis provides clear proof that Zr site of UiO-66 is dropped from electrode into the electrolyte side by formation of $[Zr_2(OH)_2(CO_3)_4]^{2-}$ during CO_2RR while Bi particles rarely fall off (Fig. S17). Due to the loss of Zr, Bi/Zr ratio from SEM-EDX analysis is also increased after 4100 s (Fig. S13). Meanwhile, Bi particles are partly segregated during CO_2 electrolysis (See Fig. S18 for SEM-EDX results and see Fig. S19 and S20 for ECSA results). It is confirmed that Bi particles after 4100 s reaction are slightly segregated than at 960 s. However, ECSA is even 1.3 times increased indicating active surface area is not decreased. For further morphological information, we finally carried out STEM-EDX analysis in comparison of 960 s and 4100 s (See Fig. S21 and S22 for the dark-field STEM image with EDX analysis maps). Bi signal was uniformly found on Zr-MOF composites for both states. However, interestingly, the Bi/UiO-66 after 960 s of CO_2RR shows Bi particles with size of about 150 $\sim$ 200 nm are interacted with the outer surface of Zr-MOF composite whereas Bi particles are missing at exterior site of Zr-MOF after 4100 s CO_2RR. That is, when the current density is decreased to 68 % after CO_2RR for 4100 s, Bi particles located at exterior site of Zr-MOF were detached and segregated with each other. Thus, these results herein imply the Bi/Zr-MOF interface promotes higher CO_2 current density.

3.4. CO_2 partial pressure dependence and proposed mechanism

We demonstrated the CO_2 electrolysis by varying the partial pressure of CO_2 ranging from 0.25 to 1.0 atm to study the effect of CO_2 partial pressure (P_{CO2}) dependency on catalytic activity (Fig. 6a and Fig. S22). Both samples with and without UiO-66 support show linearly increased j_{HCOOH} as partial CO_2 pressure increases indicating reaction order is same. However, it is definite that Bi with UiO-66 samples can convert CO_2 much more efficiently than without UiO-66. For example, in case of Bi/UiO-66, it reaches up to near -100 mA cm^{-2} even at dilute condition, $P_{CO2} = 0.5$. That is, when all analysis studies were considered, the captured CO_2 gas in the form of carbonate in transformed UiO-66 structure should be attributed to the increase of CO_2RR current density activity. Here, we propose the mechanism that how CO_2 conversion rate was improved with UiO-66 structure as described in the schematic of Fig. 6b. When the CO_2 gas flowed the surface between Bi/UiO-66 and KOH electrolyte, formed HCO_3^- via reaction (2) can react with UiO-66 releasing $[Zr_2(OH)_2(CO_3)_4]^{2-}$ as explained in reaction Eq. (1) [78]. This process can be considered as CO_2 capturing process with MOF structure transformation. Meanwhile, produced formic acid (HCOOH) on Bi catalyst surface can provide a proton via ionization nearby catalysts surface. Then, we estimated that protons can release carbonate ions like reaction Eq. (4) from Zr site to Bi catalysts side in the form of CO_2 which can be directly used for CO_2RR. Direct CO_2 conversion with carbonate electrolyte with this reaction process was also proposed by Prof. Sargent group [79]. As another to release carbonates species from Zr site, zirconium-formate compounds formation can be also considered
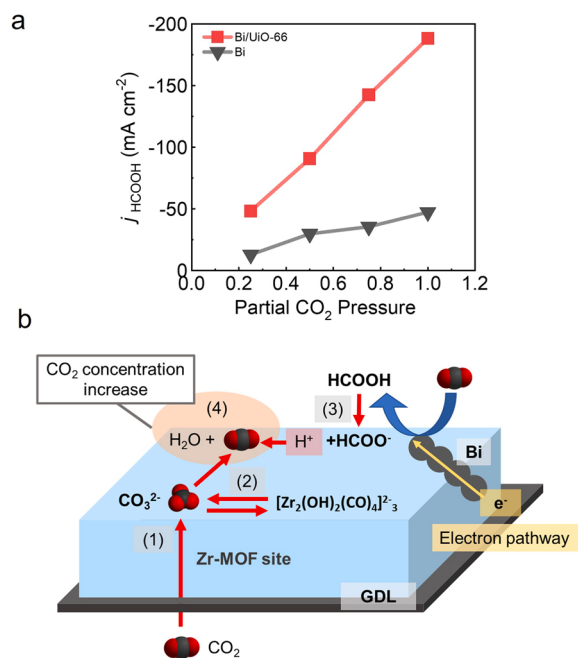
Fig. 6. (a) partial current density for HCOOH product (j_{HCOOH}) as a function of P_{CO2} for Bi/UiO-66 and only Bi samples. (b) The schematic showing the proposed mechanism for the improved CO_2 reduction activity with Bi/UiO-66 structure. In the schematic, (1) $\sim$ (4) correspond to the chemical reactions of $Zr_6O_4(OH)_4(BDC)_6 + 18HCO_3^- \rightarrow 3[Zr_2(OH)_2(CO_3)_4]^{2-} + 8 H_2O + 6CO_2 + 6BDC^{2-}$, $CO_2 + OH^- \leftrightarrow HCO_3^-$, $HCOOH \leftrightarrow H^+ + HCOO^-$ and $2CO_3^{2-} + 4 H^+ \rightarrow 2CO_2 + 2H_2O$, respectively.

[80].

$$CO_2 + OH^- \leftrightarrow HCO_3^- \tag{2}$$

$$HCOOH \leftrightarrow H^+ + HCOO^- \tag{3}$$

$$2CO_3^{2-} + 4 H^+ \rightarrow 2CO_2 + 2 H_2O \tag{4}$$

As the result of this proposed procedures, CO_2 concentration should be locally increased around the interface of Bi and UiO-66, thereby high current density can be successfully achieved in case of Bi/UiO-66. Based on our results, it is worth nothing that zirconium hydroxide compounds with carbonate species are beneficial for higher CO_2 conversion while Bi/Zr-MOF interface can efficiently promote the utilization of the carbonates. Therefore, the findings suggest the venues to explore efficient electrocatalyst design strategy with MOF support materials toward higher CO_2 conversion rate. Important issues to be addressed in future studies is the construction of stable catalysts structure and in-situ mechanistic studies for carbonate concentration for practical application.

4. Conclusion

We present the strategy to improve electrochemical CO_2 conversion activity by utilizing UiO-66 which is Zr-based MOF with Bi catalyst. It achieves 4 $\sim$ 5 times higher current density performance in the potential ranges from -0.4 to -0.7 V vs. RHE for producing HCOOH as compared to Bi alone with high HCOOH FE of 70 $\sim$ 85 %. Meanwhile, NH_2-functionalized UiO-66 does not enhance CO_2RR showing the effect of disassembled organic linker is negligible. Ex-situ FTIR and Raman spectroscopy after CO_2 reduction test at -0.7 V vs. RHE for Bi/UiO-66 sample revealed structural evolution occurs during electrolysis while characteristic peaks from UiO-66 structure disappears. It is estimated that $[Zr_2(OH)_2(CO_3)_4]^{2-}$ might be formed by chemical reaction of UiO-66 and HCO_3^- suggesting CO_2 can be captured as form of carbonate

species at Zr-MOF sites. As the results, XPS investigations shows clear evidence that carbonate species at 289.2 eV is observable when Bi/UiO-66 is still active state (j_{HCOOH}: -57 mA cm^{-2} at 960 s of CO_2 electrolysis test). However, carbonate relevant peak is missing after j_{HCOOH} for Bi/UiO-66 is declined to -40 mA cm^{-2} of j_{HCOOH} while Bi particles are detached from Zr-MOF. It indicates both carbonate species on Zr-MOF and the interface of Bi and Zr-MOF are significant for high CO_2 reduction current density. Our work provides the feasibility of Zr-MOF for CO_2 capture and conversion for high efficiency and shed lights on the application with various electrocatalysts for practical CO_2 conversion technology.

CRediT authorship contribution statement

Yuta Takaoka: Conceptualization, Methodology, Formal analysis, Investigation, Data curation, Writing – original draft. **Jun Tae Song:** Conceptualization, Methodology, Validation, Supervision, Funding acquisition, Writing – review & editing, **Atsushi Takagaki:** Validation, Manuscript checking and editing, **Motonori Watanabe:** Validation, Manuscript checking and editing, **Tatsumi Ishihara:** Supervision, Funding acquisition, Validation, Manuscript editing, Manuscript final version approval.

Declaration of Competing Interest

The authors declare the following financial interests/personal relationships which may be considered as potential competing interests: Jun Tae Song reports financial support was provided by Japan Society for the Promotion of Science. Jun Tae Song reports financial support was provided by Carbon Recycling Fund Institute.

Data Availability

Data will be made available on request.

Acknowledgements

Appendix A. Supporting information

Supplementary data associated with this article can be found in the online version at doi:10.1016/j.apcatb.2023.122400.

References

[1] B.A. Zhang, C. Costentin, D.G. Nocera, On the conversion efficiency of CO_2 electroreduction on gold, Joule 3 (2019) 1565–1568.

[2] W. Zhu, K. Zhao, S. Liu, M. Liu, F. Peng, P. An, B. Qin, H. Zhou, H. Li, Z. He, Low-overpotential selective reduction of CO_2 to ethanol on electrodeposited Cu$_x$Au$_y$ nanowire arrays, J. Energy Chem. 37 (2019) 176–182.

[3] A. Goyal, G. Marcandalli, V.A. Mints, M.T.M. Koper, Competition between CO_2 reduction and hydrogen evolution on a gold electrode under well-defined mass transport conditions, J. Am. Chem. Soc. 142 (2020) 4154–4161.

[4] Y. Yamazaki, M. Miyaji, O. Ishitani, Utilization of low-concentration CO_2 with molecular catalysts assisted by CO_2-capturing ability of catalysts, additives, or reaction media, J. Am. Chem. Soc. 144 (2022) 6640–6660.

[5] Y. Cheng, J. Hou, P. Kang, Integrated capture and electroreduction of Flue Gas CO_2 to formate using amine functionalized SnO$_x$ nanoparticles, ACS Energy Lett. 6 (2021) 3352–3358.

[6] H.J. Erick, L. Fengwang, O. Adnan, S.R. Armin, G. de, A.F. Pelayo, L. Shijie, Z. Shuzhen, L. Mingchuan, W. Xue, L. Yanwei, X. Yi, B. Koen, M.R. Kai, D. Cao-Thang, S. David, S.E.H. CO_2, electrolysis to multicarbon products in strong acid, Science 372 (2021) 1074–1078.

[7] D.H. Nam, O. Shekhah, G. Lee, A. Mallick, H. Jiang, F. Li, B. Chen, J. Wicks, M. Eddaoudi, E.H. Sargent, Intermediate binding control using metal-organic frameworks enhances electrochemical CO_2 reduction, J. Am. Chem. Soc. 142 (2020) 21513–21521.

[8] D.-H. Nam, O.S. Bushuyev, J. Li, P. de Luna, A. Seifitokaldani, C.-T. Dinh, F. P. García de Arquer, Y. Wang, Z. Liang, A.H. Proppe, C.S. Tan, P. Todorović, O. Shekhah, C.M. Gabardo, J.W. Jo, J. Choi, M.-J. Choi, S.-W. Baek, J. Kim, D. Sinton, S.O. Kelley, M. Eddaoudi, E.H. Sargent, Metal–organic frameworks mediate Cu coordination for selective CO_2 electroreduction, J. Am. Chem. Soc. 140 (2018) 11378–11386.

[9] M. Luo, Z. Wang, Y.C. Li, J. Li, F. Li, Y. Lum, D.H. Nam, B. Chen, J. Wicks, A. Xu, T. Zhuang, W.R. Leow, X. Wang, C.T. Dinh, Y. Wang, Y. Wang, D. Sinton, E. H. Sargent, Hydroxide promotes carbon dioxide electroreduction to ethanol on copper via tuning of adsorbed hydrogen, Nat. Commun. 10 (2019) 1–7.

[10] K.D. Yang, W.R. Ko, J.H. Lee, S.J. Kim, H. Lee, M.H. Lee, K.T. Nam, Morphology-directed selective production of ethylene or ethane from CO_2 on a Cu mesopore electrode, Angew. Chem. Int. Ed. 56 (2017) 796–800.

[11] P. Chauhan, K. Hiekel, J.S. Diercks, J. Herranz, V.A. Saveleva, P. Khavlyuk, A. Eychmüller, T.J. Schmidt, Electrochemical surface area quantification, CO_2 reduction performance, and stability studies of unsupported three-dimensional Au aerogels versus carbon-supported Au nanoparticles, ACS Mater. Au 2 (2021) 278–292.

[12] Y. Chen, C.W. Li, M.W. Kanan, Aqueous CO_2 reduction at very low overpotential on oxide-derived au nanoparticles, J. Am. Chem. Soc. 134 (2012) 19969–19972.

[13] J. Bok, S.Y. Lee, B.-H. Lee, C. Kim, D.L.T. Nguyen, J.W. Kim, E. Jung, C.W. Lee, Y. Jung, H.S. Lee, J. Kim, K. Lee, W. Ko, Y.S. Kim, S.-P. Cho, J.S. Yoo, T. Hyeon, Y. J. Hwang, Designing atomically dispersed Au on tensile-strained Pd for efficient CO_2 electroreduction to formate, J. Am. Chem. Soc. 143 (2021) 5386–5395.

[14] D. Gao, H. Zhou, F. Cai, J. Wang, G. Wang, X. Bao, Pd-Containing nanostructures for electrochemical CO_2 reduction reaction, ACS Catal. 8 (2018) 1510–1519.

[15] P. Deng, H. Wang, R. Qi, J. Zhu, S. Chen, F. Yang, L. Zhou, K. Qi, H. Liu, B.Y. Xia, Bismuth oxides with enhanced bismuth–oxygen structure for efficient electrochemical reduction of carbon dioxide to formate, ACS Catal. 10 (2020) 743–750.

[16] T. Fan, W. Ma, M. Xie, H. Liu, J. Zhang, S. Yang, P. Huang, Y. Dong, Z. Chen, X. Yi, Achieving high current density for electrocatalytic reduction of CO_2 to formate on bismuth-based catalysts, Cell Rep. Phys. Sci. 2 (2021), 100353.

[17] K. Xiang, Y. Liu, C. Li, X. Liu, H. Yi, L. Wu, F. Shen, M. Liu, P. Wang, H. Liu, Microenvironmental feeding and stabilization of C_2H_4 intermediates by iodide-doped copper nanowire arrays to boost C_2H_6 formation, Energy Fuels 35 (2021) 15987–15994.

[18] S.W. Chou, P.T. Chou, Alloy nanostructured catalysts for cathodic reactions in energy conversion and fuel generation, Energy Fuels 35 (2021) 18857–18870.

[19] W. Wang, R. Lu, X. Xiao, S. Gong, D.K. Sam, B. Liu, X. Lv, CuAg nanoparticle/carbon aerogel for electrochemical CO_2 reduction, N. J. Chem. (2021).

[20] Y. Yang, S. Wang, Y. Jiang, X. Wu, C. Xia, R. Peng, Y. Lu, CO_2 activation and reduction on Pt-CeO$_2$-based, Catal., J. Phys. Chem. C. 123 (2019) 17092–17101.

[21] S.-X. Guo, F. Li, L. Chen, D.R. MacFarlane, J. Zhang, Polyoxometalate-promoted electrocatalytic CO_2 reduction at nanostructured silver in dimethylformamide, ACS Appl. Mater. Interfaces 10 (2018) 12690–12697.

[22] J. Zhang, G. Zeng, L. Chen, W. Lai, Y. Yuan, Y. Lu, C. Ma, W. Zhang, H. Huang, Tuning the reaction path of CO_2 electroreduction reaction on indium single-atom catalyst: Insights into the active sites, Nano Res. 15 (2022) 4014–4022.

[23] B. Pan, G. Yuan, X. Zhao, N. Han, Y. Huang, K. Feng, C. Cheng, J. Zhong, L. Zhang, Y. Wang, Y. Li, Highly dispersed indium oxide nanoparticles supported on carbon nanorods enabling efficient electrochemical CO_2 reduction, Small Sci. 1 (2021), 2100029.

[24] L. Ma, N. Liu, B. Mei, K. Yang, B. Liu, K. Deng, Y. Zhang, H. Feng, D. Liu, J. Duan, Z. Jiang, H. Yang, Q. Li, In situ-activated indium nanoelectrocatalysts for highly active and selective CO_2 electroreduction around the thermodynamic potential, ACS Catal. 12 (2022) 8601–8609.

[25] W. Ma, S. Xie, X.G. Zhang, F. Sun, J. Kang, Z. Jiang, Q. Zhang, D.Y. Wu, Y. Wang, Promoting electrocatalytic CO_2 reduction to formate via sulfur-boosting water activation on indium surfaces, Nat. Commun. 10 (2019) 1–10.

[26] W. Yu, L. Wen, J. Gao, S. Chen, Z. He, D. Wang, Y. Shen, S. Song, Facile treatment tuning the morphology of Pb with state-of-the-art selectivity in CO_2 electroreduction to formate, Chem. Commun. 57 (2021) 7418–7421.

[27] J.E. Pander, J.W.J. Lum, B.S. Yeo, The importance of morphology on the activity of lead cathodes for the reduction of carbon dioxide to formate, J. Mater. Chem. A 7 (2019) 4093–4101.

[28] Y. Chen, M.W. Kanan, Tin oxide dependence of the CO_2 reduction efficiency on tin electrodes and enhanced activity for tin/tin oxide thin-film catalysts, J. Am. Chem. Soc. 134 (2012) 1986–1989.

[29] M.F. Baruch, J.E. Pander, J.L. White, A.B. Bocarsly, Mechanistic insights into the reduction of CO_2 on tin electrodes using in situ ATR-IR spectroscopy, ACS Catal. 5 (2015) 3148–3156.

[30] J.-X. Wu, X.-R. Zhu, T. Liang, X.-D. Zhang, S.-Z. Hou, M. Xu, Y.-F. Li, Z.-Y. Gu, Sn (101) derived from metal–organic frameworks for efficient electrocatalytic reduction of CO_2, Inorg. Chem. 60 (2021) 9653–9659.

[31] F. Cai, D. Gao, H. Zhou, G. Wang, T. He, H. Gong, S. Miao, F. Yang, J. Wang, X. Bao, Electrochemical promotion of catalysis over Pd nanoparticles for CO_2 reduction, Chem. Sci. 8 (2017) 2569–2573.

[32] B. Jiang, X.G. Zhang, K. Jiang, D.Y. Wu, W. bin Cai, Boosting formate production in electrocatalytic CO_2 reduction over wide potential window on Pd surfaces, J. Am. Chem. Soc. 140 (2018) 2880–2889.

[33] W. Ma, J. Bu, Z. Liu, C. Yan, Y. Yao, N. Chang, H. Zhang, T. Wang, J. Zhang, Monoclinic scheelite bismuth vanadate derived bismuthene nanosheets with rapid kinetics for electrochemically reducing carbon dioxide to formate, Adv. Funct. Mater. 31 (2021), 2006704.

[34] F. Yang, A.O. Elnabawy, R. Schimmenti, P. Song, J. Wang, Z. Peng, S. Yao, R. Deng, S. Song, Y. Lin, M. Mavrikakis, W. Xu, Bismuthene for highly efficient carbon dioxide electroreduction reaction, Nat. Commun. 11 (2020) 1088.

[35] P. Su, W. Xu, Y. Qiu, T. Zhang, X. Li, H. Zhang, Ultrathin bismuth nanosheets as a highly efficient CO₂ reduction electrocatalyst, ChemSusChem 11 (2018) 848–853.

[36] S.H. Yoon, G. Piao, H. Park, N.O. Elbashir, D.S. Han, Theoretical insight into effect of cation–anion pairs on CO₂ reduction on bismuth electrocatalysts, Appl. Surf. Sci. 532 (2020), 147459.

[37] N. Li, P. Yan, Y. Tang, J. Wang, X.-Y. Yu, H. bin Wu, In-situ formation of ligand-stabilized bismuth nanosheets for efficient CO₂ conversion, Appl. Catal. B 297 (2021), 120481.

[38] Q. Gong, P. Ding, M. Xu, X. Zhu, M. Wang, J. Deng, Q. Ma, N. Han, Y. Zhu, J. Lu, Z. Feng, Y. Li, W. Zhou, Y. Li, Structural defects on converted bismuth oxide nanotubes enable highly active electrocatalysis of carbon dioxide reduction, Nat. Commun. 10 (2019) 2807.

[39] K. Fan, Y. Jia, Y. Ji, P. Kuang, B. Zhu, X. Liu, J. Yu, Curved surface boosts electrochemical CO₂ reduction to formate via bismuth nanotubes in a wide potential window, ACS Catal. 10 (2020) 358–364.

[40] W. Lv, J. Zhou, J. Bei, R. Zhang, L. Wang, Q. Xu, W. Wang, Electrodeposition of nano-sized bismuth on copper foil as electrocatalyst for reduction of CO₂ to formate, Appl. Surf. Sci. 393 (2017) 191–196.

[41] S.-X. Guo, Y. Zhang, X. Zhang, C.D. Easton, D.R. MacFarlane, J. Zhang, Phosphomolybdic acid-assisted growth of ultrathin bismuth nanosheets for enhanced electrocatalytic reduction of CO₂ to formate, ChemSusChem 12 (2019) 1091–1100.

[42] M. Miola, B.C.A. de Jong, P.P. Pescarmona, An efficient method to prepare supported bismuth nanoparticles as highly selective electrocatalyst for the conversion of CO₂ into formate, Chem. Commun. 56 (2020) 14992–14995.

[43] D. Wu, J. Liu, Y. Liang, K. Xiang, X.-Z. Fu, J.-L. Luo, Electrochemical transformation of facet-controlled BiOI into mesoporous bismuth nanosheets for selective electrocatalytic reduction of CO₂ to formic acid, ChemSusChem 12 (2019) 4700–4707.

[44] H. Xie, T. Zhang, R. Xie, Z. Hou, X. Ji, Y. Pang, S. Chen, M.-M. Titirici, H. Weng, G. Chai, Facet engineering to regulate surface states of topological crystalline insulator bismuth rhombic dodecahedrons for highly energy efficient electrochemical CO₂ reduction, Adv. Mater. 33 (2021), 2008373.

[45] Y. Isaka, Y. Kawase, Y. Kuwahara, K. Mori, H. Yamashita, Two-phase system utilizing hydrophobic metal–organic frameworks (MOFs) for photocatalytic synthesis of hydrogen peroxide, Angew. Chem. Int. Ed. 58 (2019) 5402–5406.

[46] Q. Liang, S. Cui, C. Liu, S. Xu, C. Yao, Z. Li, Construction of CdS@UiO-66-NH₂ core-shell nanorods for enhanced photocatalytic activity with excellent photostability, J. Colloid Interface Sci. 524 (2018) 379–387.

[47] L. Shen, S. Liang, W. Wu, R. Liang, L. Wu, Multifunctional NH₂-mediated zirconium metal–organic framework as an efficient visible-light-driven photocatalyst for selective oxidation of alcohols and reduction of aqueous Cr(vi), Dalton Trans. 42 (2013) 13649–13657.

[48] F. Yu, X. Jing, Y. Wang, M. Sun, C. Duan, Hierarchically porous metal–organic framework/MoS₂ interface for selective photocatalytic conversion of CO₂ with H₂O into CH₃COOH, Angew. Chem. Int. Ed. 60 (2021) 24849–24853.

[49] Y. Fu, J. Wu, R. Du, K. Guo, R. Ma, F. Zhang, W. Zhu, M. Fan, Temperature modulation of defects in NH₂-UiO-66 (Zr) for photocatalytic CO₂ reduction, RSC Adv. 9 (2019) 37733–37738.

[50] Y. Lee, S. Kim, J.K. Kang, S.M. Cohen, Photocatalytic CO₂ reduction by a mixed metal (Zr/Ti), mixed ligand metal–organic framework under visible light irradiation, Chem. Commun. 51 (2015) 5735–5738.

[51] W. Liu, G. Zhao, M. An, L. Chang, Solvothermal synthesis of nanostructured BiVO₄ with highly exposed (010) facets and enhanced sunlight-driven photocatalytic properties, Appl. Surf. Sci. 357 (2015) 1053–1063.

[52] N. Al-Janabi, P. Hill, L. Torrente-Murciano, A. Garforth, P. Gorgojo, F. Siperstein, X. Fan, Mapping the Cu-BTC metal–organic framework (HKUST-1) stability envelope in the presence of water vapour for CO₂ adsorption from flue gases, Chem. Eng. J. 281 (2015) 669–677.

[53] Y. Sun, C. Song, X. Guo, Y. Liu, Concurrent manipulation of out-of-plane and regional in-plane orientations of NH₂-UiO-66 membranes with significantly reduced anisotropic grain boundary and superior H₂/CO₂ separation performance, ACS Appl. Mater. Interfaces 12 (2020) 4494–4500.

[54] B. Koyuturk, C. Altintas, F.P. Kinik, S. Keskin, A. Uzun, Improving gas separation performance of ZIF-8 by [BMIM][BF₄] incorporation: interactions and their, Conséq. Perform., J. Phys. Chem. C. 121 (2017) 10370–10381.

[55] D. Narváez-Celada, A.S. Varela, CO₂ electrochemical reduction on metal–organic framework catalysts: current status and future directions, J. Mater. Chem. A 10 (2022) 5899–5917.

[56] H. Zhong, M. Ghorbani-Asl, K.H. Ly, J. Zhang, J. Ge, M. Wang, Z. Liao, D. Makarov, E. Zschech, E. Brunner, I.M. Weidinger, J. Zhang, et al., Synergistic electroreduction of carbon dioxide to carbon monoxide on bimetallic layered conjugated metal-organic frameworks, Nat. Commun. 11 (2020) 1–10.

[57] K. Samson, M. Sliwa, R.P. Socha, K. Góra-Marek, D. Mucha, D. Rutkowska-Zbik, J. F. Paul, M. Ruggiero-Mikoajczyk, R. Grabowski, J. Soczyński, Influence of ZrO₂ structure and copper electronic state on activity of Cu/ZrO₂ catalysts in methanol synthesis from CO₂, ACS Catal. 4 (2014) 3730–3741.

[58] J.B. Decoste, G.W. Peterson, H. Jasuja, T.G. Glover, Y.G. Huang, K.S. Walton, Stability and degradation mechanisms of metal–organic frameworks containing the Zr₆O₄(OH)₄ secondary building unit, J. Mater. Chem. A 1 (2013) 5642–5650.

[59] Y. Zhao, Q. Zhang, Y. Li, R. Zhang, G. Lu, Large-scale synthesis of monodisperse UiO-66 crystals with tunable sizes and missing linker defects via acid/base Co-modulation, ACS Appl. Mater. Interfaces 9 (2017) 15079–15085.

[60] J.T. Song, H. Song, B. Kim, J. Oh, Towards higher rate electrochemical CO₂ conversion: from liquid-phase to gas-phase systems, Catalysts 9 (2019) 224.

[61] F. Song, X. Hu, Exfoliation of layered double hydroxides for enhanced oxygen evolution catalysis, Nat. Commun. 5 (2014) 4477.

[62] X. Zhang, Y. Zhang, T. Wang, Z. Fan, G. Zhang, A thin film nanocomposite membrane with pre-immobilized UiO-66-NH₂ toward enhanced nanofiltration performance, RSC Adv. 9 (2019) 24802–24810.

[63] J. Ding, Z. Yang, C. He, X. Tong, Y. Li, X. Niu, H. Zhang, UiO-66(Zr) coupled with Bi₂MoO₆ as photocatalyst for visible-light promoted dye degradation, J. Colloid Interface Sci. 497 (2017) 126–133.

[64] I. Strauss, K. Chakarova, A. Mundstock, M. Mihaylov, K. Hadjiivanov, N. Guschanski, J. Caro, UiO-66 and UiO-66-NH₂ based sensors: dielectric and FTIR investigations on the effect of CO₂ adsorption, Microporous Mesoporous Mater. 302 (2020), 110227.

[65] J. Shanahan, D.S. Kissel, E. Sullivan, PANI@UiO-66 and PANI@UiO-66-NH₂ polymer-MOF hybrid composites as tunable semiconducting materials, ACS Omega 5 (2020) 6395–6404.

[66] M. Laporta, M. Pegoraro, L. Zanderighi, Perfluorosulfonated membrane (Nafion): FT-IR study of the state of water with increasing humidity, Phys. Chem. Chem. Phys. 1 (1999) 4619–4628.

[67] Z. Liang, W. Chen, J. Liu, S. Wang, Z. Zhou, W. Li, G. Sun, Q. Xin, FT-IR study of the microstructure of Nafion® membrane, J. Membr. Sci. 233 (2004) 39–44.

[68] S. Ryu, J.H. Kim, J.Y. Lee, S.H. Moon, Investigation of the effects of electric fields on the nanostructure of Nafion and its proton conductivity, J. Mater. Chem. A 6 (2018) 20836–20843.

[69] H. Veisi, M. Abrifam, S.A. Kamangar, M. Pirhayati, S.G. Saremi, M. Noroozi, T. Tamoradi, B. Karmakar, Pd immobilization biguanidine modified Zr-UiO-66 MOF as a reusable heterogeneous catalyst in Suzuki–Miyaura coupling, Sci. Rep. 11 (2021) 1–14.

[70] Y. Fang, L. Zhang, Q. Zhao, X. Wang, X. Jia, Highly selective visible-light photocatalytic benzene hydroxylation to phenol using a new heterogeneous photocatalyst UiO-66-NH₂-SA-V, Catal. Lett. 149 (2019) 2408–2414.

[71] J. Yang, Y. Dai, X. Zhu, Z. Wang, Y. Li, Q. Zhuang, J. Shi, J. Gu, Metal–organic frameworks with inherent recognition sites for selective phosphate sensing through their coordination-induced fluorescence enhancement effect, J. Mater. Chem. A 3 (2015) 7445–7452.

[72] H.L. Cha, J. il Yun, Redox behaviors of zirconium in molten LiCl-KCl eutectic salt based on the comproportionation reaction between Zr(0) and Zr(IV), Electrochem. Commun. 84 (2017) 86–89.

[73] Z. Sun, T. Ma, H. Tao, Q. Fan, B. Han, Fundamentals and challenges of electrochemical CO₂ reduction using two-dimensional materials, Chem 3 (2017) 560–587.

[74] J. Chu, F.-S. Ke, Y. Wang, X. Feng, W. Chen, X. Ai, H. Yang, Y. Cao, Facile and reversible digestion and regeneration of zirconium-based metal-organic frameworks, Commun. Chem. 3 (2020) 5.

[75] R.B. Balow, J.G. Lundin, G.C. Daniels, W.O. Gordon, M. McEntee, G.W. Peterson, J. H. Wynne, P.E. Pehrsson, Environmental effects on zirconium hydroxide nanoparticles and chemical warfare agent decomposition: implications of atmospheric water and carbon dioxide, ACS Appl. Mater. Interfaces 9 (2017) 39747–39757.

[76] F. Takasaki, K. Fujiwara, Y. Nakajima, T. Nishikawa, H. Masu, M. Imanari, Y. Hidaka, N. Ogawa, A monomeric [Zr(CO₃)₄]⁴⁻ complex in an ammonium zirconium carbonate aqueous solution studied by extended X-ray absorption fine structure, Raman and nuclear magnetic resonance spectroscopy, Dalton. Trans. 44 (2014) 645–652.

[77] S.R. Teeparthi, E.W. Awin, R. Kumar, Dominating role of crystal structure over defect chemistry in black and white zirconia on visible light photocatalytic activity, Sci. Rep. 8 (2018) 5541.

[78] X. Lu, C. Zhu, Z. Wu, J. Xuan, J.S. Francisco, H. Wang, In situ observation of the pH gradient near the gas diffusion electrode of CO₂ reduction in alkaline electrolyte, J. Am. Chem. Soc. 142 (2020) 15438–15444.

[79] Y.C. Li, G. Lee, T. Yuan, Y. Wang, D.H. Nam, Z. Wang, F.P. Garciá De Arquer, Y. Lum, C.T. Dinh, O. Voznyy, E.H. Sargent, C.O.2 Electroreduction from carbonate electrolyte, ACS Energy Lett. 4 (2019) 1427–1431.

[80] J.I. Choi, H. Chun, M.S. Lah, Zirconium-formate macrocycles and supercage: molecular Packing versus MOF-like network for water vapor sorption, J. Am. Chem. Soc. 140 (2018) 10915–10920.